GEOPHYSICS, VOL. 79, NO. 2 (MARCH-APRIL 2014); P. F1–F10, 10 FIGS., 2 TABLES.
10.1190/GEO2013-0270.1

Mapping crustal thickness using marine gravity data: Methods and uncertainties

Yongliang Bai[1], Simon E. Williams[2], R. Dietmar Müller[2], Zhan Liu[3], and Maral Hosseinpour[2]

ABSTRACT

Crustal thickness is a critical parameter for understanding the processes of continental rifting and breakup and the evolution of petroleum systems within passive margins. However, direct measurements of crustal thickness are sparse and expensive, highlighting the need for methodologies using gravity anomaly data, jointly with other geophysical data, to estimate crustal thickness. We evaluated alternative gravity inversion methodologies to map crustal thickness variations at rifted continental margins and adjacent oceanic basins, and we tested our methodology in the South China Sea (SCS). Different strategies were investigated to estimate and remove the gravity effect of density variations of sediments and the temperature and pressure variations of the lithospheric mantle from the observed free air gravity anomaly data. Sediment density was calculated using a relationship between sediment thickness, porosity, and density. We found that this method is essential for crustal thickness inversion in the presence of a thick sedimentary cover by comparing the Moho depths obtained from gravity inversion and seismic interpretation in the Yinggehai Basin where sediments are up to 13 km thick; the inversion accuracy depended on the parameters of the exponential equation between porosity and the buried depth. We modeled the lithospheric mantle temperature field based on oceanic crustal age, continental crustal stretching factors, and other boundary conditions. We tested three different methods to calculate the thermal expansion coefficient, which is either held constant or is a linear/polynomial function of temperature, for applying a thermal correction and found that the inversion results were relatively insensitive to alternative methods. We compared inversion results with two recent deep seismic profiles that image the rifted continental edge at the northern margin of the SCS and the continental Liyue Bank (Reed Bank) at the southern margin, and we found that the inversion accuracy was improved considerably by removing sediment, thermal, and pressure gravity effects.

INTRODUCTION

Crustal thickness varies significantly across continental margins, and mapping these variations is important for understanding continental rifting processes (Reston and Morgan, 2004; Huismans and Beaumont, 2011; Sutra and Manatschal, 2012), the hydrocarbon habitats within these regions (Unternehr et al., 2010), as well as subduction systems (Kind et al., 2002). The Moho delineates the boundary between crust and mantle (Lewis, 1983), and this interface can be imaged accurately through expensive deep seismic profiling, but economic considerations make gravity modeling a more practical approach for mapping crustal thickness over regional scales. To isolate the gravity anomaly caused only by the geometry of the Moho interface, all other contributions to the free air gravity anomaly must be removed. The accuracy of Moho depth inversion depends on how accurately the removal of these other gravity anomaly sources can be achieved. More and more deep seismic profiles are being collected over continental margins, even though the quality of seismic interpretation is affected by the data acquisition and processing, the accuracy of the seismic interpretation should be better than the gravity inversion on the whole. Therefore, gravity inversion results can be compared with deep seismic interpretations, allowing the gravity inversion accuracy to be evaluated quantitatively.

Manuscript received by the Editor 17 July 2013; revised manuscript received 15 October 2013; published online 6 March 2014.
[1]China University of Petroleum (East China), School of Geosciences, Qingdao, China and University of Sydney, School of Geosciences, EarthByte Group, New South Wales, Australia. E-mail: yongliang.bai1986@gmail.com.
[2]University of Sydney, School of Geosciences, EarthByte Group, New South Wales, Australia. E-mail: simon.williams@sydney.edu.au; dietmar.muller@sydney.edu.au; maral.hosseinpour@sydney.edu.au.
[3]China University of Petroleum (East China), School of Geosciences, Qingdao, China. E-mail: liuzhan@upc.edu.cn.

The density of sediments is dependent on the grain density as well as the porosity. Porosity is affected by the overlying sediment thickness and is the main property that affects bulk sediment density (Sawyer, 1985). Thus, sediment density is not constant with depth.

Present-day lithospheric mantle density decreases with depth when the thermal expansion effect is stronger than the compression effect driven by overburden stress at relatively shallow depths; the density increases with depth when the pressure effect is dominant (Kimbell et al., 2004). The density change caused by thermal expansion can produce a large thermal gravity anomaly, which may reach −320 mGal in new oceanic lithospheric mantle and remains large at rifted continental margins (Chappell and Kusznir, 2008). The density change due to compression driven by overburden stress is also not negligible (Afonso et al., 2008).

For these reasons, assuming uniform sediment density and uniform lithospheric mantle density is likely to be insufficient for gravity inversion in many cases. Instead, all gravity effects due to density variations within the sediments and due to temperature and pressure variations within the lithospheric mantle should be taken into consideration to get accurate crust thickness by gravity inversion. In this study, we present a workflow that incorporates all these elements and quantitatively assess the limitations of the different assumptions inherent within our approach.

We evaluate the methodology by application to the South China Sea (SCS). There are many basins in the SCS, their sedimentary fill is thick due to substantial crustal extension and thermal subsidence (Wheeler and White, 2000; Yan et al., 2001; Clift et al., 2002), and the SCS is a magma-poor young marginal sea (Yan et al., 2006). Also, there are many interpreted deep seismic profiles in SCS area, which can be used for validating the gravity inversion accuracy. (In addition to our manuscript, we provide a full set of MATLAB scripts and functions that will allow readers to reproduce our results or apply the methodology to other areas.)

METHODOLOGY

In the marine realm, the free air gravity anomaly (g_{faa}) is the sum of several components:

$$g_{faa} = g_{mra} + g_b + g_s + g_t + g_p + g_o, \tag{1}$$

where g_{mra} is the mantle residual anomaly, g_b is the anomaly due to lateral changes of bathymetry, g_s is the gravity effect of the sediment layer, g_t is the gravity anomaly that originates from density variations because of thermal expansion, g_p is the gravity anomaly from density changes by pressure compression, and g_o is the gravity field caused by the other sources, for example, igneous intrusions. The mantle residual anomaly due to the geometry of the Moho interface is

$$g_{mra} = g_{faa} - g_b - g_s - g_t - g_p - g_o. \tag{2}$$

In this paper, the geologic model is composed of four main parts: water layer, sediment layer, crust, and conduction-dominated lithospheric mantle. The gravity effect of each layer is estimated by Fourier domain forward modeling methods (Parker, 1973; Blakely, 1995). The seawater density is set to a uniform value of 1.03 g/cm^3 for removing the seawater gravity effect. The density distribution within the other layers is determined as part of the workflow, as discussed in the following sections.

Sediment density

Estimating the gravity effect of the sediment depends on knowledge of how the thickness of the sediment varies laterally and the density distribution within the sediment layer. One relationship between sediment porosity (Φ_z) and overlying sediment thickness (z) (Sclater and Christie, 1980; Sawyer, 1985) is

$$\Phi_z = \Phi_0 e^{-cz}, \tag{3}$$

where Φ_0 is the initial sediment porosity at the seabed, c is an empirically determined constant with units 1/depth. If sedimentary pore space is filled by seawater, with z km overlying sediment, the density (ρ_z) will be (Sawyer, 1985)

$$\rho_z = \Phi_z \rho_w + (1 - \Phi_z)\rho_{sg}, \tag{4}$$

where ρ_w is the seawater density and ρ_{sg} is the grain density. ρ_{sg} is set at 2.65 g/cm^3 generally, for example, by Sawyer (1985) and López-Coto et al. (2013).

Lithospheric mantle density: Thermal effect

The temperature field of the oceanic lithospheric mantle is generally estimated from the variation of depth and heat flow with crustal age. It uses a simple analytic model for a cooling plate that assumes the thermal expansion coefficient (TEC), the thermal conductivity, and the initial temperature are constant (McKenzie et al., 2005). Several methods have been proposed for oceanic lithospheric mantle temperature calculation, for example, by McKenzie (1978), Parsons and Richter (1980), Bouhifd et al. (1996), McKenzie et al. (2005), and Afonso et al. (2008).

The pure shear model (McKenzie, 1978) can be used for stretched continental lithospheric mantle and also for old oceanic lithospheric mantle (Chappell and Kusznir, 2008). We use it for calculating the temperature field of the lithospheric mantle as follows:

$$T = T_1 \left[1 - \frac{z}{a} + \frac{2}{\pi} \sum_{n=1}^{\infty} \frac{(-1)^{n+1}}{n} \left[\frac{\gamma}{n\pi} \sin \frac{n\pi}{\gamma} \right] \times \exp\left(\frac{n^{-2} t}{\tau} \right) \sin \frac{n\pi z}{a} \right], \tag{5}$$

where T_1 is the bottom temperature, z is the vertical distance from the target point to the model basement, a is the depth to the base of the model, γ is the lithospheric stretching factor, and t is the crustal age. Appropriate values for T_1, a, and τ are 1060 K, 125 km, and 62.8 Myr, respectively (McKenzie, 1978; McKenzie et al., 2005).

The oceanic crustal age can be interpreted from marine magnetic lineations, and it is usually much younger than the continental crustal age. To get a smooth temperature field between the oceanic and continental lithospheric mantle, we assume a transition zone surrounding the oceanic crust. The first iteration without thermal and pressure correction yields an initial guess of the crustal thickness, and then the crustal age is linearly interpolated within the transition zone, which is contained by the crustal thickness predicted by the previous iteration. The crustal age of this zone transits from the

oceanic crustal age to the continental crustal age gradually from its ocean side to landward; thus, the thermal and pressure correction can be added. In the pure shear model, the lithospheric stretching factor equals the continental crustal stretching factor (McKenzie, 1978). The continental crustal stretching factor (γ) equals tc_0/tc_{now}, tc_0 is the initial crustal thickness before stretching, and tc_{now} is the present-day crustal thickness. For the oceanic area, $\gamma = \infty$, and for the unstretched continental area, $\gamma = 1$.

When the temperature is T, the lithospheric mantle density affected by thermal expansion is

$$\rho_T = \rho_0[1 - \alpha(T)(T - T_0)], \tag{6}$$

where ρ_0 is the mantle density with normal temperature T_0 and normal pressure P_0 and it is set at 3.3 g/cm^3 in this paper, P_0 is the standard atmospheric pressure, T_0 is 273 K, and $\alpha(T)$ is the TEC when the temperature is T. The unit for temperature is K, and for α, it is K^{-1}.

Some authors take α as a constant (3.28×10^{-5} K^{-1}) for any depth/temperature (Parsons and Sclater, 1977; Chappell and Kusznir, 2008). Bouhifd et al. (1996) come to the conclusion that the TEC of forsterite increases smoothly from 2.8 to 4.5 K^{-1} when the temperature rises from 400 to 2160 K ($\alpha = 2.83 \times 10^{-5} + 7.58 \times 10^{-9}$ T), according to a powder X-ray diffraction experiment with synchrotron radiation. Kroll et al. (2012) simulate the TEC with several equations, and the $\alpha - T$ curve is not linear when the temperature is lower than 600 K. We fit the $\alpha - T$ curve for forsterite from Kroll et al. (2012) with the polynomial function of temperature

$$\alpha_T = (6 \times 10^{-10}\ \mathrm{T}^3 - 2 \times 10^{-6}\ \mathrm{T}^2 + 0.0039\ \mathrm{T} + 1.727) \times 10^{-5}. \tag{7}$$

Lithospheric mantle density: Pressure effect

The compressibility coefficient β is a measure of the relative volume change as a response to pressure compression, and it has a reciprocal relationship with the bulk modulus K. Its value is affected by temperature:

$$\beta_T = -\frac{1}{V}\left(\frac{\partial V}{\partial P}\right)_T = \frac{1}{K_T}, \tag{8}$$

where $(\frac{\partial V}{\partial P})_T$ is the volume difference according to pressure change when the temperature is T. Based on petrophysics experiments, Bouhifd et al. (1996) argue that $\alpha_T K_T \approx 3.98$ MPaK^{-1} at high temperature. Kroll et al. (2012) simulate the bulk modulus as a function of temperature for forsterite:

$$K_T = 127.97 - 0.0232(T - 300), \tag{9}$$

where the unit of K_T is GPa, and for T, it is K.

The density difference $\Delta\rho_P$ caused by pressure change $(P(z) - P_0)$ at temperature T is

$$\Delta\rho_P = \rho_0\beta_T[P(z) - P_0], \tag{10}$$

where ρ_0 and P_0 have been described by equation 6, the $P(z)$ is the pressure on the target point where the temperature is T. The unit for temperature is K, for pressure, it is MPa, and for β, it is MPa^{-1}.

In this paper, we assume that the composition of the lithospheric mantle does not vary with depth. At relatively shallow depths, the temperature of the oceanic lithospheric mantle with a relatively young crustal age increases with depth much more quickly than at older ages, if only affected by thermal expansion. The temperature reaches 1600 K at 125 km for each curve (Figure 1a); the oceanic lithospheric mantle density decreases to 3.16 g/cm^3 at 125 km depth with different density-depth curves for different crustal ages (Figure 1b). After accounting for the pressure effect, the density decreases for shallower levels and then increases as the depth within the lithosphere increases, reaching 3.24 g/cm^3 at 125 km depth (Figure 1b). There is a considerable density difference between the assumption of mantle lithospheric density being only affected by thermal expansion and by thermal expansion and pressure-driven compression.

Gravity inversion

There are several inversion methods for calculating the topography of the Moho interface from the mantle residual gravity anomaly. We use the Fourier domain method of Oldenburg (1974) because it is relatively fast in terms of computation time. The main inversion workflow is shown in Figure 2. At the beginning, an appropriate value range of different possible values is set for each parameter in three kinds of correction models (sediment density variation, thermal expansion, and pressure effect), and also for the reference Moho depth d_0 and crustal density ρ_c. For the first iteration, after the seawater and sediment gravity effect has been removed, we set the density of the entire lithospheric mantle as

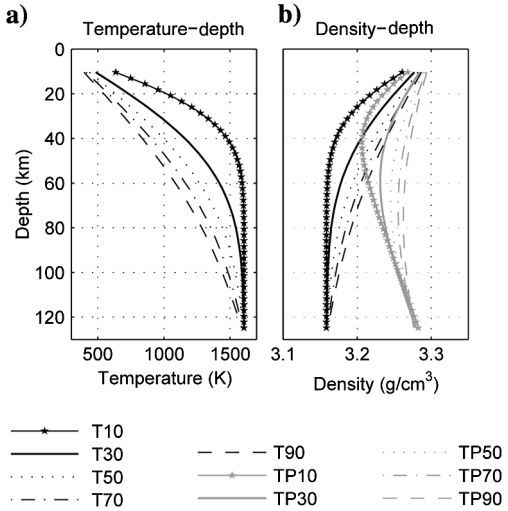

Figure 1. (a) Temperature-depth curves of the oceanic lithospheric mantle with different crustal ages based on the pure shear model (equation 5); each item in the legend with prefix 'T' followed by a number stands for the temperature curve with specific crustal ages. (b) Oceanic lithospheric mantle density-depth curves with different crustal ages; each item in the legend with prefix 'T' takes thermal expansion into consideration, and prefix 'P' takes the pressure-driven compression into consideration. In the legends, the number for each item stands for oceanic crustal age.

3.3 g/cm^3 without removing thermal and pressure effects. The initial continental crustal thickness is derived from seismic profiles and/or receiver functions. We calculate the stretching factor for thinned continental crust. In the next stage, we calculate the Moho interface again including thermal and pressure correction, and then we modify the transition area and stretching factor with the new result based on these corrections. We then repeat the workflow and take its result as the final crustal thickness.

The calculated Moho interface depends on initial assumptions of crustal density (which controls the density contrast across the Moho) and the reference depth. The most appropriate values for these parameters are unknown at the start of the process. Results are calculated for a range of combinations of parameters within reasonable bounds. We compare each of these inversion results with deep seismic profiles; the one with the smallest rms (between the Moho depths from interpreted seismic profiles and the Moho depths from gravity inversion at the same sampling stations) is the best combination for the target area.

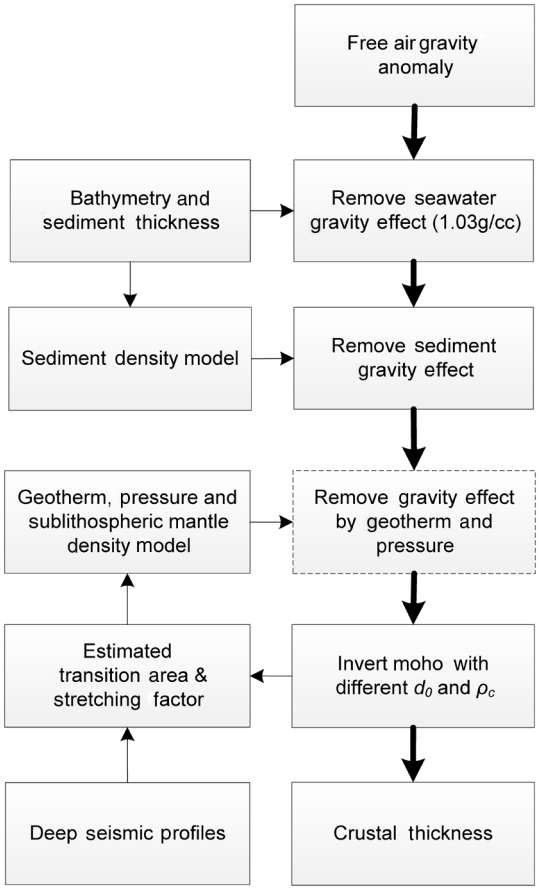

Figure 2. Moho depth inversion flow; the main part is assigned with thick arrows, d_0 is the reference Moho depth, and ρ_c is the crustal density. This flow should be executed with all possible combinations of parameter values. The gravity field is much more sensitive to the shallow objects than the deep objects, and the reference Moho depth reflects the average depth of the Moho interface. The crustal density will affect the density contrast between the crust and the lithospheric mantle; thus, the reference Moho depth and the crustal density are the important input parameters for gravity inversion.

CASE STUDY AT SOUTH CHINA SEA

Geologic background

The northern margin of the proto-SCS was formed in the Middle Jurassic as a convergent Andean-type continental margin, including the North Palawan Block and the Liyue Bank (Reed Bank) (Hilde et al., 1977; Taylor and Hayes, 1983; Lüdmann and Wong, 1999). The India-Asia collision resulted in a strike-slip fault, the Red River Fault, which contributed to the opening of the SCS (Briais et al., 1993; Lee and Lawver, 1994; Clift et al., 2008). South China continental block rifting started from Palaeocene and seafloor spreading initiated ~32 Ma and lasted up to ~16 million years (Taylor and Hayes, 1980, 1983; Briais et al., 1993). The onset of seafloor spreading within the SCS was diachronous, with opening initially starting in the eastern region and progressively propagating westward (Hayes and Nissen, 2005). The initial spreading center was located at the northern margin of the Reed Bank (Li and Song, 2012; Zhu et al., 2012); there was also a southward ridge jump at ~25 Ma (Hall, 1997; Ding et al., 2011) (Figure 3).

At present, the SCS is bounded to the north by the passive South China continental margin (Nissen and Hayes, 1995), to the east by the Manila trench where oceanic crust of the SCS is being subducted eastward beneath the Luzon Arc (Zhu et al., 2012), to the south by the microcontinental blocks of Liyue Bank (Reed Bank) and Dangerous Grounds, which were stretched at the beginning and compressed later (Taylor and Hayes, 1980, 1983; Nissen and Hayes, 1995; Franke et al., 2011), and to the west by the Indo-China shelf (Kido et al., 2001; Shi et al., 2003) (Figure 3).

The western part of the northern margin was much more extended than the eastern part. Hayes and Nissen (2005) suggest that the most likely causes of the differences in rift history are east–west variations in the rheology of the prerift crust and associated west–east variations in the geothermal structure of the prerift lithosphere. From west to east, there are several basins: Qiongdongnan Basin, Pearl River Mouth Basin, and Taixinan Basin (Figure 3). Each basin has a thick sedimentary layer with thicknesses varying from 6 to 10 km. The sediment thickness in the Yinggehai Basin reaches 13 km (Divins, 2004).

Crustal thickness inversion

Our gravity inversion is based on global offshore free air gravity anomaly data (Sandwell and Smith, 2009) (v20.1), and it follows the workflow shown in Figure 2. We calculate gravity corrections as discussed above using the GEBCO global bathymetry compilation grid (http://www.bodc.ac.uk/projects/international/gebco/gebco_digital_atlas), the NGDC global sediment thickness map for the oceans. This sediment thickness grid was compiled from three principle sources: the previously published isopach map, ocean drilling results, and seismic reflection profiles (Divins, 2004). The grid describes the depth to the acoustic basement, so it represents a minimum estimate of the sediment thickness (Divins, 2004). Figure 4 shows the comparison of the depth of the sediment basement from seismic interpretation and the NGDC grid along the profiles where the sediment basement was interpreted (Table 1), and their total rms is 1.34 km. The thermal correction was calculated using the oceanic crustal age grid (Müller et al., 2008; Seton et al., 2012); we digitized published deep seismic profiles (Table 1) and Moho depths from

receiver functions (Figure 3) to provide constraints on the gravity inversion results.

We use seismic profiles located at the north and south margins of the SCS (Table 1 and Figure 3). Although we consider the Moho depths indicated by refraction studies to be better constrained than estimates from gravity data, these estimates still contain uncertainties that must be considered. On the intersection point between SP-4 and SP-6 near the north–west subbasin (Figure 3), the Moho depth from SP-6 is 19.4 km, and from SP-4, it is 22.9 km; thus, the difference is 3.5 km; the Moho depth difference between SP-6 and SP-5 on their intersection point is 2 km. Hence, there is a substantial interpretation misfit between these seismic profiles.

Our 3D sediment thickness model has a 50 m vertical resolution and a 5×5 km horizontal resolution. The sediment density for each grid of the model is calculated according to equations 3 and 4.

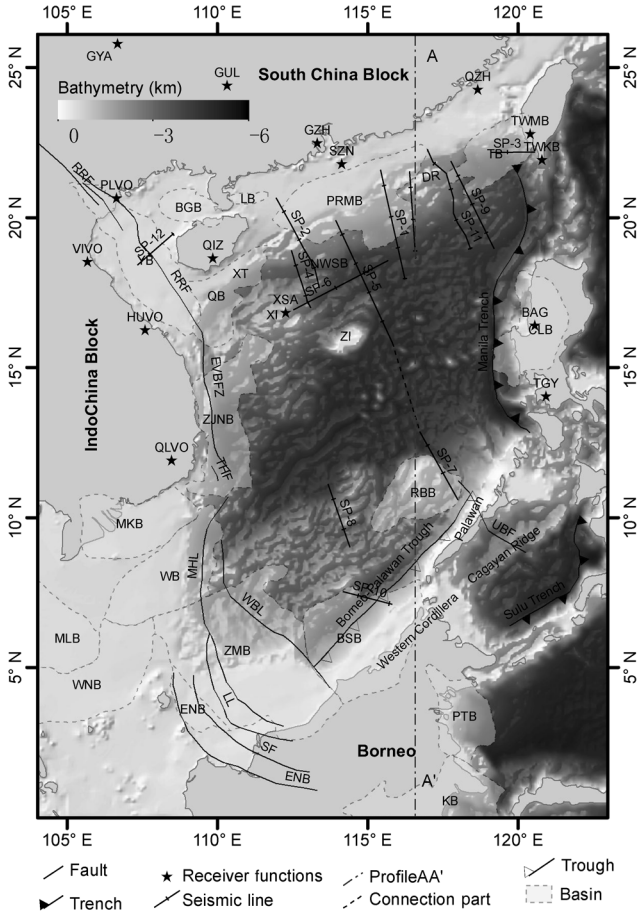

Figure 3. Simplified structural map showing tectonic setting of the SCS and its adjacent area (after Mazur et al., 2012). The base map is the GEBCO global bathymetry and topography compilation grid. Sedimentary basins: BB, Beibuwan Basin; BSB, Brunei-Sabah Basin; CLB, Central Luzon Basin; ENB, East Natuna Basin; KB, Kutei Basin; LB, Leidong Basin; MKB, Mekong Basin; MLB, Malay Basin; PRMB, Pearl River Mouth Basin; PTB, Pamusian Tarakan Basin; QB, Qiongdongnan Basin; RBB, Reed Bank Basin; TB, Taixinan Basin; WB, Wanan Basin; WNB, West Natuna Basin; YB, Yinggehai Basin; ZJNB, Zhongjiannan Basin; ZMB, Zengmu Basin. Faults: EVBFZ, East Vietnam Boundary Fault Zone; LL, Lupar Line; MHL, Mukah Line; RRF, Red River Fault; SF, Sebangkai Fault; THF, Tuy Hoa Fault; UBF, Ulugan Bay Fault; and WBL, West Baram Line.

The gravity effect of thermal expansion and pressure changes driven by overburden stress within the lithospheric mantle is obtained by a 3D grid model with 5 km resolution in all directions. The initial unstretched crustal thickness is set to 31 km according to the crustal thickness beneath several stations of receiver function on offshore South China continental block (GYA, 38 km; CNS, 30 km; NNC, 28 km; GUL, 30 km; WZH, 28 km; QZH 30 km; GZH, 28 km; and QIZ, 33 km, from Tkalčić et al., 2011). Within the continents, the crustal age is set as 300 Myr, and the boundary of the transition zone is spanned by crustal thicknesses between 9.3 and 21.7 km, the crustal thickness values used here derived by the gravity inversion in the traditional way (the crustal density is 2.8 g/cm^3, and the mantle density is 3.3 g/cm^3), and the crustal thickness values can be revised after adding the thermal expansion and pressure-driven compression correction. Figure 5 shows the final inversion result of the crustal thickness of SCS.

DISCUSSIONS

In the following sections, we discuss how the gravity inversion result is influenced by different parameters of each correction model. This illustrates the relative importance of the different choices made in the initial parameters on the final, best-fitting Moho depth.

Gravity effect of sediment layer

To investigate the importance of the depth-density function for sedimentary layers and the sensitivity of the inversion result to the parameters of this function, we generated results assuming such a function with different values of (Φ_0, c) (Table 2) and assuming a uniform sediment density of 2.3 g/cm^3. The root mean square (rms) between the Moho depths at the sampling stations (with 5 km interval) from seismic interpretation and gravity inversion is used for evaluating the sediment correction accuracy. The values of Φ_0 and c can be obtained through fitting the measurement data by equation 3. There are three ocean drilling program (ODP) sites in

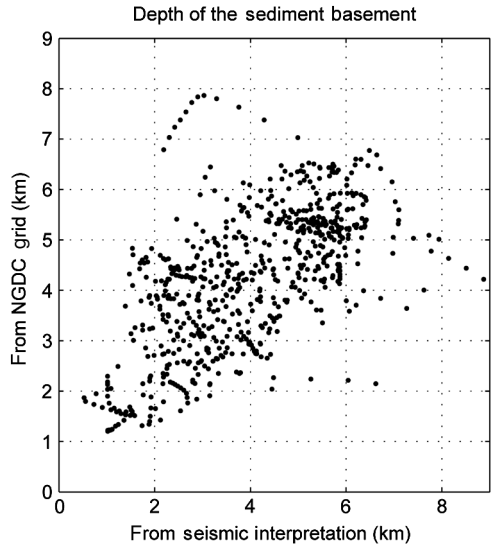

Figure 4. The plot map between the depth of the sediment basement from seismic interpretation and the NGDC grid along the profiles where the sediment basement was interpreted (Table 1).

the SCS region, and their values of Φ_0, c are (0.63, 5.1), (0.49, 2.7), and (0.70, 7.1) separately (Clift et al., 2002). Table 2 shows the density calculation result and gravity inversion accuracy by different values of Φ_0, c of equations 3 and 4 for sediment correction along the profile SP12, which is located in the Yinggehai Basin, and the thickest sediment layer along this profile reaches 13 km. When using these three different groups of values, the sediment densities at the bottom of the sediment layer are similar but the sediment densities at the top of the sediment layer are much different, and this difference results in different inversion accuracy. Therefore, the inversion accuracy depends on the parameters of the exponential equation between porosity and the buried depth.

The smallest rms is 0.41 km when the gravity inversion is based on the parameters from ODP site 3 ($\Phi_0 = 0.70, c = 7.1$), and it is 2.1 km when the gravity inversion is based on constant sediment density (2.3 g/cm^3), much larger than the former one (Figure 6). These results suggest that using a depth-density function to estimate the gravity effect of sedimentary layers yields significantly more reliable estimates of Moho depth from gravity inversion.

Gravity effect of thermal expansion and pressure compression

Figure 7 illustrates the variations in the temperature and pressure field and their effects on the density distribution within the lithospheric mantle and gravity field, extracted as vertical cross sections from the 3D volume along profile AA′ (Figure 3). Along profile AA′ (Figure 7), the density decrease by thermal expansion reaches 141.5 kg/m^3, and the biggest relative thermal gravity anomaly is 192.93 mGal; the density increase by pressure compression reaches 110.6 kg/m^3, and the biggest relative pressure gravity anomaly is 30.0 mGal. The pressure field, which is relatively smooth, induces a relatively flat density change, resulting in small-amplitude changes in the gravity field. Thus, the biggest relative pressure gravity anomaly (30.0 mGal) is much smaller than the biggest relative thermal gravity anomaly (192.93 mGal). Comparing to the gravity

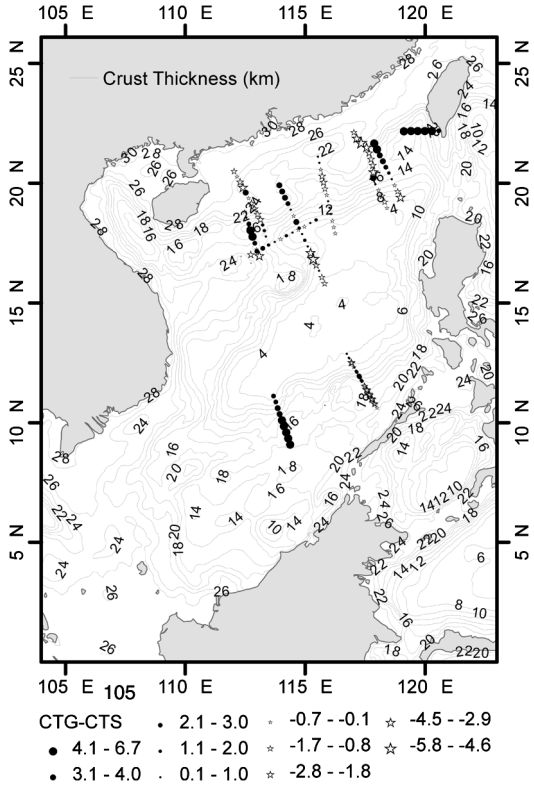

Figure 5. Crustal thickness map of SCS from gravity inversion based comprehensive corrections and the difference between the crustal thickness from gravity inversion and seismic interpretation. CTG-CTS is the resulting crust thickness from gravity inversion minus the crust thickness from seismic interpretation. The parameters for inversion are decided based on the discussion part: Set TEC as constant (3.28×10^{-5} K^{-1}); the compressibility coefficient is from the linear function of temperature (equation 9).

Table 1. Main seismic profiles used by this study (seismic profile type: OBS, ocean bottom seismic; ESP, expanding spread profile; and OBH, ocean bottom hydrophone).

Name	Profile type	Year	Length (km)	Margin	Reference	Was sediment basement interpreted?
SP-1	OBS	1993	410	North	Yan et al. (2001)	Yes
SP-2	ESP	1985	395	North	Hayes and Nissen (2005)	Yes
SP-3	OBS	1995	150	North	McIntosh et al. (2005)	Yes
SP-4	OBH	1996	220	North	Qiu et al. (2001)	Yes
SP-5	OBS	2006	480	North	Li (2011)	Yes
SP-6	OBS	2006	380	North	Ao et al. (2012)	Yes
SP-7	OBS	2009	360	North	Li (2011)	Yes
SP-8	OBS	2009	250	North	Hao et al. (2011)	Yes
SP-9	OBS	2001	350	South	Wang et al. (2006)	Yes
SP-10	—	2001	185	South	Franke et al. (2008)	Yes
SP-11	ESP	1985	410	South	Hayes and Nissen (2005)	Yes
SP-12	OBH	1996–1997	170	Yinggehai Basin	Liu et al. (2011)	No

anomaly by thermal expansion, the gravity anomaly by pressure-driven compression is relatively small; the pressure field and the density change by pressure-driven compression is much smoother than the temperature field and the density change by thermal expansion. The gravity anomaly field by thermal expansion is relatively smooth along the continent and continental margins and gets its high value on the oceanic basin. Therefore, we can expect gravity effects of this scale and amplitude to have a significant influence on estimates of the Moho undulations especially on the oceanic areas.

Comparison with seismic profiles

We vary the crust density from 2.6 to 3.0 g/cm^3 and the reference Moho depth from 18 to 38 km for the gravity inversion. The seismic interpretation results are fixed, and the Moho depth is calculated with each combination of (ρ_c, d_0). Then we compare the difference between seismic interpretation and the inversion result; the inversion result is affected by the crustal density and the reference Moho depth (Figure 8). To get the best combination of (ρ_c, d_0), we create the rms plot between the seismic interpretation and the inversion result (Figure 9).

Three different methods are used to calculate TEC for thermal correction, and the inversion results with these corrections are compared with the interpreted seismic refraction Moho (Figure 9). As noted earlier, the considerable discrepancy exists between crossing seismic profiles — Both of these profiles are used in the

Table 2. Density calculation result and gravity inversion accuracy by different values of Φ_0,c of equations 3 and 4 for sediment correction along profile SP12 (ρ_{st}, sediment density at the top of the sediment layer; ρ_{sb}, sediment density at the bottom of the sediment layer; rms, the root mean square between the Moho interface along this profile obtained by seismic interpretation and the gravity inversion with specific values of Φ_0,c from each ODP site).

	Site 1	Site 2	Site 3
Φ_0	0.63	0.49	0.70
C (10^{-4}/m)	5.10	2.70	7.10
ρ_{st} g/cm^3	1.66	1.87	1.56
ρ_{sb} (g/cm^3)	2.65	2.63	2.65
rms (km)	0.48	0.86	0.41

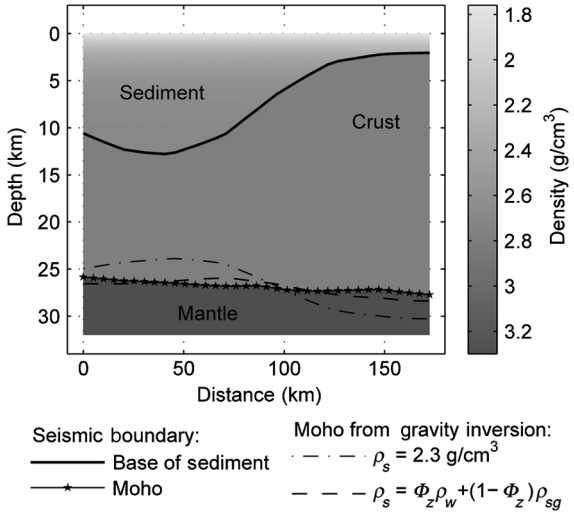

Figure 6. Profile along SP-12 in the Yinggehai Basin (Figure 3), which illustrates the density for each layer and the different layer interfaces. The seawater along this profile is shallower than 60 m, and it is not rendered. Colors present the density for each layer, and the left color bar shows the density value.

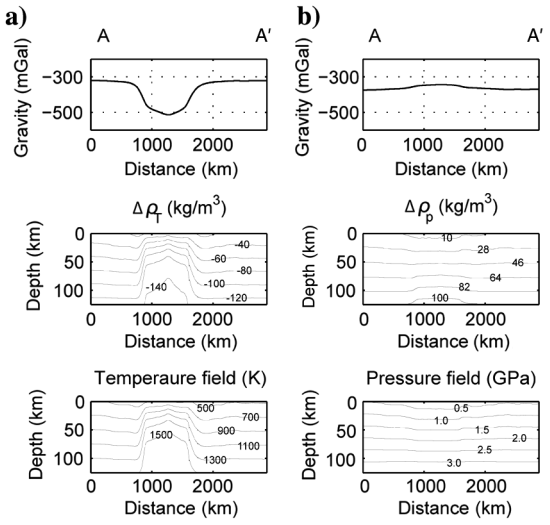

Figure 7. Thermal expansion and pressure-driven compression effect along profile AA′ (Figure 3). (a) Temperature field (bottom), density change by thermal expansion (medium), and gravity anomaly by thermal expansion (top). (b) Pressure field (bottom), the density change by pressure-driven compression (medium), and gravity anomaly by pressure-driven compression (top).

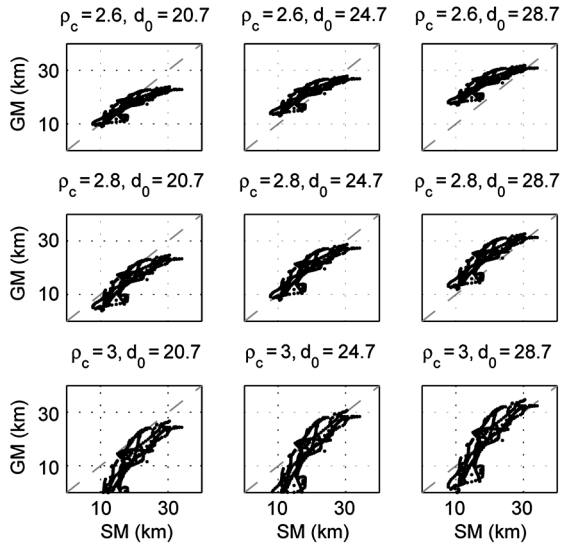

Figure 8. The plot map between the Moho depth from seismic interpretation and from gravity inversion with all the corrections mentioned formerly. SM is the Moho depth from seismic, GM is the Moho depth from gravity inversion, ρ_c is the crust density (g/cm3), and d_0 is the reference Moho depth (km).

comparison, limiting the possibility for a single gravity inversion surface to fit all the seismic constraints and so limiting the minimum possible rms. Finally, there are very similar rms contour maps for the gravity inversion based on three different kinds of TEC calculating methods and adding pressure correction in addition to thermal correction (Figure 9). The seismic lines used in this study are concentrated on the continental margins, which makes it difficult to assess different results for the deep ocean basin (rms plots are similar with and without adding a pressure correction in addition to a thermal correction for the basin flanks).

For assessing the inversion accuracy in the oceanic basin, in Figure 10 we compare gravity inversion results with interpreted seismic data along the two recent OBS seismic profiles; parts of these profiles are located in the oceanic basin (Figure 3). With an assumption of uniform density for the mantle, the Moho depth from gravity inversion is underestimated at the landward edge of the profile and overestimated within oceanic areas (Figure 10). Adding thermal correction can make the inversion result fit the seismic interpretation result much better on the continent but also the oceanic area. Adding a pressure correction in addition to a thermal correction produces relatively small differences to the best-fitting crustal thickness estimate across the continental margins (Figures 9 and 10) and a relatively noticeable difference within oceanic regions (Figure 10).

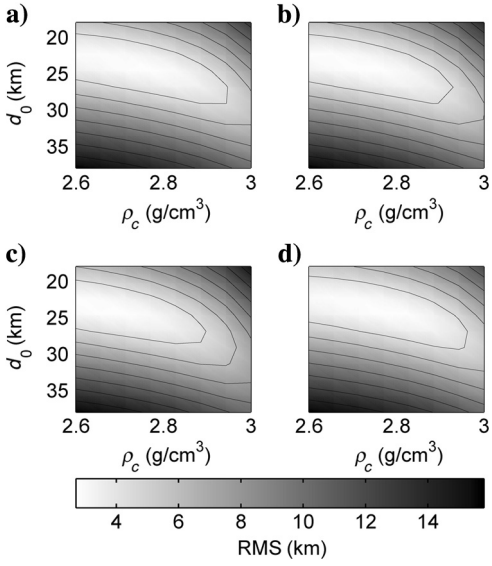

Figure 9. In the rms rendered map, color represents the rms between the Moho depths from seismic interpretation and gravity inversions, the black lines are rms contours, ρ_c is the crust density, and d_0 is the reference Moho depth. (a) Thermal correction is based on constant TEC (3.28×10^{-5} K^{-1}), and without pressure correction, its minimum rms is 2.7 km ($\rho_c = 2.77$ g/cm^3, $d_0 = 24.67$ km). (b) Thermal correction is based on assuming TEC as a linear function of temperature ($\alpha = 2.83 \times 10^{-5} + 7.58 \times 10^{-9}$ T), and without pressure correction, its minimum rms is 2.8 km ($\rho_c = 2.77$ g/cm^3, $d_0 = 24.67$ km). (c) Thermal correction is based on taking TEC as a polynomial function of temperature (equation 7), and without pressure correction, its minimum rms is 2.8 km ($\rho_c = 2.71$ g/cm^3, $d_0 = 24.67$ km). (d) Thermal correction is based on constant TEC (3.28×10^{-5} K^{-1}), and also with pressure correction, its minimum rms is 2.7 km ($\rho_c = 2.77$ g/cm^3, $d_0 = 24.67$ km).

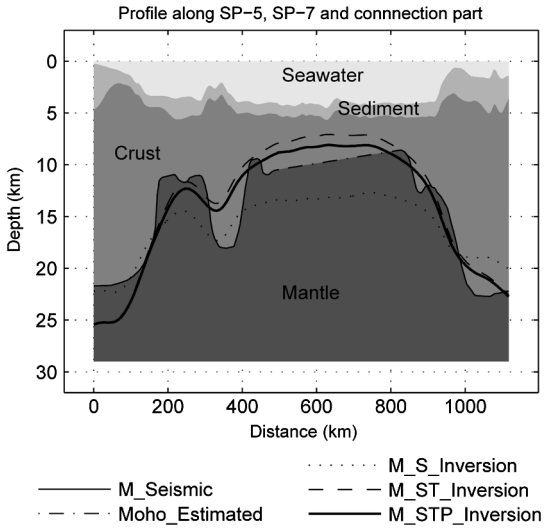

Figure 10. Profile starting from the northern margin of SCS and ending at the southern continental Liyue Bank (Reed Bank), which connects seismic lines SP-5 and SP-7 (Figure 3). There is no seismic profile along the connection part; we connect the Moho point at the end of SP-5 to the Moho point at the beginning of SP-7 with a straight dashed line. Each item of legend with prefix M stands for the Moho interface. M_S_Inversion is the Moho interface from gravity inversion based on its best parameters ($\rho_c = 2.70$ g/cm^3, $d_0 = 24.67$) with sediment correction but without thermal and pressure correction. M_ST_Inversion is the Moho interface from gravity inversion based on its best parameters ($\rho_c = 2.77$ g/cm^3, $d_0 = 24.67$) with sediment and thermal correction (constant TEC) but without pressure correction. M_STP_Inversion is the Moho interface from gravity inversion based on its best parameters ($\rho_c = 2.77$ g/cm^3, $d_0 = 24.67$) with sediment, thermal, and pressure correction.

CONCLUSION

We review the methods for removing gravity anomalies related to sediment thickness, thermal expansion, and pressure compression from the free air gravity anomaly. We then explore the influence of these factors on gravity-derived estimates of Moho depth and discuss the sensitivity of the results to different parameters. We apply this methodology to map the crustal thickness in the SCS and compare a range of results with seismic refraction observations.

The sediment gravity effect can be removed more accurately with depth-density functions for sedimentary layers than with constant sediment density, and the accuracy depends on the parameters of the exponential equation between porosity and the buried depth.

The inversion accuracy is similar with assuming TEC as constant (3.28×10^{-5} K^{-1}), a linear function ($\alpha = 2.83 \times 10^{-5} + 7.58 \times 10^{-9}$ T), or a polynomial function of temperature. The constant model is the preferable one for thermal correction due to its simplicity and accuracy.

Variations in temperature, and to a lesser extent variations in pressure due to overburden stress, influence the density distribution within the lithospheric mantle and cause long-wavelength gravity anomalies. Adding thermal correction produces a much more reliable result on the continental margin and also on the oceanic area; adding pressure correction in addition to the thermal correction cannot improve the inversion accuracy significantly because the pressure field is relatively smooth.

ACKNOWLEDGMENTS

This work is supported by the China Scholarship Council, the Fundamental Research Funds for the Central Universities (no. 12CX06001A), and ARC grant no. FL0992245.

REFERENCES

Afonso, J. C., M. Fernàndez, G. Ranalli, W. L. Griffin, and J. A. D. Connolly, 2008, Integrated geophysical-petrological modeling of the lithosphere and sublithospheric upper mantle: Methodology and applications: Geochemistry, Geophysics, Geosystems, **9**, Q05008, doi: 10.1029/2007GC001834.

Ao, W., M. Zhao, X. Qiu, A. Ruan, and J. Li, 2012, Crustal structure of the northwest sub-basin of the South China Sea and its tectonic implication: Earth Science — Journal of China University of Geosciences, (in Chinese) **37**, 779–790, doi: 10.3799/dqkx.2012.087.

Blakely, R., 1995, Potential theory in gravity and magnetic applications: Cambridge University Press.

Bouhifd, M. A., D. Andrault, G. Fiquet, and P. Richet, 1996, Thermal expansion of forsterite up to the melting point: Geophysical Research Letters, **23**, 1143–1146, doi: 10.1029/96GL01118.

Briais, A., P. Patriat, and P. Tapponnier, 1993, Updated interpretation of magnetic anomalies and seafloor spreading stages in the South China Sea: Implications for the tertiary tectonics of Southeast Asia: Journal of Geophysical Research, **98**, 6299–6328, doi: 10.1029/92JB02280.

Chappell, A. R., and N. J. Kusznir, 2008, Three-dimensional gravity inversion for Moho depth at rifted continental margins incorporating a lithosphere thermal gravity anomaly correction: Geophysical Journal International, **174**, 1–13, doi: 10.1111/j.1365-246X.2008.03803.x.

Clift, P., G. H. Lee, N. Anh Duc, U. Barckhausen, H. Van Long, and S. Zhen, 2008, Seismic reflection evidence for a dangerous grounds miniplate: No extrusion origin for the South China Sea: Tectonics, **27**, TC3008, doi: 10.1029/2007TC002216.

Clift, P., J. Lin, and U. Barckhausen, 2002, Evidence of low flexural rigidity and low viscosity lower continental crust during continental break-up in the South China Sea: Marine and Petroleum Geology, **19**, 951–970, doi: 10.1016/S0264-8172(02)00108-3.

Ding, W., M. Li, L. Zhao, A. Ruan, and Z. Wu, 2011, Cenozoic tectonosedimentary characteristics and extension model of the Northwest Subbasin, South China Sea: Geoscience Frontiers, **2**, 509–517, doi: 10.1016/j.gsf.2011.05.010.

Divins, D. L., 2004, Total sediment thickness of the world's oceans and marginal seas, http://www.ngdc.noaa.gov/mgg/sedthick/sedthick.html, NOAA National Geophysical Data Center.

Franke, D., U. Barckhausen, N. Baristeas, M. Engels, S. Ladage, R. Lutz, J. Montano, N. Pellejera, E. G. Ramos, and M. Schnabel, 2011, The continent-ocean transition at the southeastern margin of the South China Sea: Marine and Petroleum Geology, **28**, 1187–1204, doi: 10.1016/j.marpetgeo.2011.01.004.

Franke, D., U. Barckhausen, I. Heyde, M. Tingay, and N. Ramli, 2008, Seismic images of a collision zone offshore NW Sabah/Borneo: Marine and Petroleum Geology, **25**, 606–624, doi: 10.1016/j.marpetgeo.2007.11.004.

Hall, R., 1997, Cenozoic plate tectonic reconstructions of SE Asia: Geological Society, London, Special Publications, **126**, 11–23, doi: 10.1144/GSL.SP.1997.126.01.03.

Hao, T., Y. Xu, F. Sun, Q. You, and C. Lu, 2011, Integrated geophysical research on the tectonic attribute of conjugate continental margin of South China Sea: Chinese Journal of Geophysics, **54**, 988–1008, doi: 10.1002/cjg2.1679.

Hayes, D. E., and S. S. Nissen, 2005, The South China sea margins: Implications for rifting contrasts: Earth and Planetary Science Letters, **237**, 601–616, doi: 10.1016/j.epsl.2005.06.017.

Hilde, T. W. C., S. Uyeda, and L. Kroenke, 1977, Evolution of the western Pacific and its margin: Tectonophysics, **38**, 145–165, doi: 10.1016/0040-1951(77)90205-0.

Huismans, R., and C. Beaumont, 2011, Depth-dependent extension, two-stage breakup and cratonic underplating at rifted margins: Nature, **473**, 74–78, doi: 10.1038/nature09988.

Kido, Y., K. Suyehiro, and H. Kinoshita, 2001, Rifting to spreading process along the northern continental margin of the South China Sea: Marine Geophysical Researches, **22**, 1–15, doi: 10.1023/A:1004869628532.

Kimbell, G. S., R. W. Gatliff, J. D. Ritchie, A. S. D. Walker, and J. P. Williamson, 2004, Regional three-dimensional gravity modelling of the NE Atlantic margin: Basin Research, **16**, 259–278, doi: 10.1111/j.1365-2117.2004.00232.x.

Kind, R., X. Yuan, J. Saul, D. Nelson, S. V. Sobolev, J. Mechie, W. Zhao, G. Kosarev, J. Ni, U. Achauer, and M. Jiang, 2002, Seismic images of crust and upper mantle beneath Tibet: Evidence for Eurasian plate subduction: Science, **298**, 1219–1221, doi: 10.1126/science.1078115.

Kroll, H., A. Kirfel, R. Heinemann, and B. Barbier, 2012, Volume thermal expansion and related thermophysical parameters in the Mg,Fe olivine solid-solution series: European Journal of Mineralogy, **24**, 935–956, doi: 10.1127/0935-1221/2012/0024-2235.

Lee, T.-Y., and L. A. Lawver, 1994, Cenozoic plate reconstruction of the South China Sea region: Tectonophysics, **235**, 149–180, doi: 10.1016/0040-1951(94)90022-1.

Lewis, B. T. R., 1983, The process of formation of ocean crust: Science, **220**, 151–157, doi: 10.1126/science.220.4593.151.

Li, C. F., and T. R. Song, 2012, Magnetic recording of the Cenozoic oceanic crustal accretion and evolution of the South China Sea basin: Chinese Science Bulletin, **57**, 1879–1895, doi: 10.1007/s11434-012-5063-9.

Li, J., 2011, Dynamics of the continental margins of South China Sea: Scientific experiments and research progresses: Chinese Journal of Geophysics, **54**, 2293–3003, doi: 10.3969/j.issn.0001-5733.2011.12.002.

Liu, S. J., G. P. Zeng, X. L. Qiu, and G. Fu, 2011, The crustal profile and onshore–offshore seismic exploration in the marine area southwest to Hainan Island: Progress in Geophysics, **26**, 922–933, doi: 10.3969/j.issn.1004-2903.2011.03.018.

López-Coto, I., J. L. Mas, and J. P. Bolivar, 2013, A 40-year retrospective European radon flux inventory including climatological variability: Atmospheric Environment, **73**, 22–33, doi: 10.1016/j.atmosenv.2013.02.043.

Lüdmann, T., and H. K. Wong, 1999, Neotectonic regime on the passive continental margin of the northern South China Sea: Tectonophysics, **311**, 113–138, doi: 10.1016/S0040-1951(99)00155-9.

Mazur, S., C. Green, M. G. Stewart, J. M. Whittaker, S. Williams, and R. Bouatmani, 2012, Displacement along the Red River Fault constrained by extension estimates and plate reconstructions: Tectonics, **31**, TC5008, doi: 10.1029/2012TC003174.

McIntosh, K., Y. Nakamura, T. K. Wang, R. C. Shih, A. Chen, and C. S. Liu, 2005, Crustal-scale seismic profiles across Taiwan and the western Philippine Sea: Tectonophysics, **401**, 23–54, doi: 10.1016/j.tecto.2005.02.015.

McKenzie, D., 1978, Some remarks on the development of sedimentary basins: Earth and Planetary Science Letters, **40**, 25–32, doi: 10.1016/0012-821X(78)90071-7.

McKenzie, D., J. Jackson, and K. Priestley, 2005, Thermal structure of oceanic and continental lithosphere: Earth and Planetary Science Letters, **233**, 337–349, doi: 10.1016/j.epsl.2005.02.005.

Müller, R. D., M. Sdrolias, C. Gaina, and W. R. Roest, 2008, Age, spreading rates, and spreading asymmetry of the world's ocean crust: Geochemistry, Geophysics, Geosystems, **9**, Q04006, doi: 10.1029/2007GC001743.

Nissen, S. S., and D. E. Hayes, 1995, Gravity, heat flow, and seismic constraints on the processes of crustal extension: Northern margin of the South China Sea: Journal of Geophysical Research, **100**, 447–483, doi: 10.1029/95JB01868.

Oldenburg, D. W., 1974, The inversion and interpretation of gravity anomalies: Geophysics, **39**, 526–536, doi: 10.1190/1.1440444.

Parker, R. L., 1973, The rapid calculation of potential anomalies: Geophysical Journal of the Royal Astronomical Society, **31**, 447–455, doi: 10.1111/j.1365-246X.1973.tb06513.x.

Parsons, B., and F. M. Richter, 1980, A relation between the driving force and geoid anomaly associated with mid-ocean ridges: Earth and Planetary Science Letters, **51**, 445–450, doi: 10.1016/0012-821X(80)90223-X.

Parsons, B., and J. G. Sclater, 1977, An analysis of the variation of ocean floor bathymetry and heat flow with age: Journal of Geophysical Research, **82**, 803–827, doi: 10.1029/JB082i005p00803.

Qiu, X., S. Ye, S. Wu, X. Shi, D. Zhou, K. Xia, and E. R. Flueh, 2001, Crustal structure across the Xisha Trough, northwestern South China Sea: Tectonophysics, **341**, 179–193, doi: 10.1016/S0040-1951(01)00222-0.

Reston, T. J., and J. P. Morgan, 2004, Continental geotherm and the evolution of rifted margins: Geology, **32**, 133–136, doi: 10.1130/G19999.1.

Sandwell, D. T., and W. H. F. Smith, 2009, Global marine gravity from retracked Geosat and ERS-1 altimetry: Ridge segmentation versus spreading rate: Journal of Geophysical Research: Solid Earth, **114**, B01411, doi: 10.1029/2008JB006008.

Sawyer, D. S., 1985, Total tectonic subsidence: A parameter for distinguishing crust type at the U.S. Atlantic Continental Margin: Journal of Geophysical Research: Solid Earth, **90**, 7751–7769, doi: 10.1029/JB090iB09p07751.

Sclater, J. G., and P. A. F. Christie, 1980, Continental stretching: An explanation of the post-mid-Cretaceou subsidence of the central North Sea basin: Journal of Geophysical Research, **85**, 3711–3739, doi: 10.1029/JB085iB07p03711.

Seton, M., R. D. Müller, S. Zahirovic, C. Gaina, T. Torsvik, G. Shephard, A. Talsma, M. Gurnis, M. Turner, S. Maus, and M. Chandler, 2012, Global continental and ocean basin reconstructions since 200 Ma: Earth-Science Reviews, **113**, 212–270, doi: 10.1016/j.earscirev.2012.03.002.

Shi, X., X. Qiu, K. Xia, and D. Zhou, 2003, Characteristics of surface heat flow in the South China Sea: Journal of Asian Earth Sciences, **22**, 265–277, doi: 10.1016/S1367-9120(03)00059-2.

Sutra, E., and G. Manatschal, 2012, How does the continental crust thin in a hyperextended rifted margin? Insights from the Iberia margin: Geology, **40**, 139–142, doi: 10.1130/G32786.1.

Taylor, B., and D. E. Hayes, 1980, The tectonic evolution of the South China Basin: American Geophysical Union, Geophysical Monograph Series, vol. 23, 89–104.

Taylor, B., and D. E. Hayes, 1983, Origin and history of the South China Sea Basin: American Geophysical Union, Geophysical Monograph Series, vol. 27, 23–56

Tkalčić, H., Y. Chen, R. Liu, H. Zhibin, L. Sun, and W. Chan, 2011, Multi-step modelling of teleseismic receiver functions combined with constraints from seismic tomography: Crustal structure beneath southeast China: Geophysical Journal International, **187**, 303–326, doi: 10.1111/j.1365-246X.2011.05132.x.

Unternehr, P., G. Péron-Pinvidic, G. Manatschal, and E. Sutra, 2010, Hyper-extended crust in the South Atlantic: In search of a model: Petroleum Geoscience, **16**, 207–215, doi: 10.1144/1354-079309-904.

Wang, T. K., M.-K. Chen, C.-S. Lee, and K. Xia, 2006, Seismic imaging of the transitional crust across the northeastern margin of the South China Sea: Tectonophysics, **412**, 237–254, doi: 10.1016/j.tecto.2005.10.039.

Wheeler, P., and N. White, 2000, Quest for dynamic topography: Observations from Southeast Asia: Geology, **28**, 963–966, doi: 10.1130/0091-7613(2000)28<963:QFDTOF>2.0.CO;2.

Yan, P., H. Deng, H. Liu, Z. Zhang, and Y. Jiang, 2006, The temporal and spatial distribution of volcanism in the South China Sea region: Journal of Asian Earth Sciences, **27**, 647–659, doi: 10.1016/j.jseaes.2005.06.005.

Yan, P., D. Zhou, and Z. Liu, 2001, A crustal structure profile across the northern continental margin of the South China Sea: Tectonophysics, **338**, 1–21, doi: 10.1016/S0040-1951(01)00062-2.

Zhu, J., X. Qiu, H. Kopp, H. Xu, Z. Sun, A. Ruan, J. Sun, and X. Wei, 2012, Shallow anatomy of a continent–ocean transition zone in the northern South China Sea from multichannel seismic data: Tectonophysics, **554–557**, 18–29, doi: 10.1016/j.tecto.2012.05.027.